Article

Journal of
Nanoscience and Nanotechnology
Vol. 14, 1–8, 2014
www.aspbs.com/jnn

Surface Characteristics, Biodegradability and Biocompatibility of Porous Silicon for Microfabricated Neural Electrode

Tao Sun[1,*], Wei Mong Tsang[1], Woo-Tae Park[1,2], and Srinivas Merugu[1]

[1] *Institute of Microelectronics, Agency for Science, Technology and Research (A*STAR), Singapore*
[2] *Department of Mechanical and Automotive Engineering, Seoul National University of Science and Technology, Seoul, Republic of Korea*

Porous Si (PSi) used for microfabrication of a novel neural electrode was prepared on Si wafers by an anodization process. Surface morphology and porous structure of the PSi were characterized using scanning electron microscopy (SEM) and transmission electron microscopy (TEM). 3D interconnected and nano sized pores were homogeneously formed across the surface. Wettability of the PSi was determined using a sessile drop method. Although Si–H_x functional groups on the PSi surface had negative effect on wettability, water contact angle of the PSi reduced to $34.5 \pm 0.5°$ due to the enhanced surface roughness and the capillary force generated by nano sized pores. Moreover, *in vitro* biocompatibility of the PSi was assessed by seeding a breast cancer cell line (MCF-7). After 5 days of culture, cell morphology was observed using a fluorescence microscope. Although more than 99% of the cells under the microscope were living for both Si and PSi samples, morphology of the cells attached on their surfaces was different. MTT assay was also used to quantitatively evaluate *in vitro* biocompatibility, and revealed false positive results due to the spontaneous reduction of MTT on the PSi surface. Therefore, MTT assay was not suitable for *in vitro* quantitatively study of PSi.

Keywords: Neural Interface, Neural Electrode, Porous Silicon, Biodegradation, Biocompatibility.

1. INTRODUCTION

As an alternative therapy to treat patients suffering from paralysis, fully implantable neural microelectrodes are used to record neuron activities from brain, and the lost motor function of the patients can be restored via decoding recorded neural signals to control external robotic devices and realize the intended motions.[1–3] After being implanted two 96-channel intracortical microelectrodes and subsequent 13-week training, a tetraplegic patient was able to freely move a prosthetic limb to perform 7-dimensional movements without adverse events.[4] However, one of major bottlenecks to limit the widespread clinical applications of the neural microelectrodes is to establish a stable neural interface between the delicate cortical tissue and conventional rigid silicon (Si) electrode. Reactive tissue response to foreign materials was triggered after the electrode insertion into the cortical tissue, and a dense and fibrous sheath was progressively formed around the microelectrode and insulated it from nearby neurons, resulting in degradation of signal quality and eventual device failure. Moreover, the brain micromotion, as a consequence of cardiac rhythm, fluctuations in respiratory pressure, head and/or trunk displacements, etc., causes the relative micromotion of the neural microelectrode.[5] Accordingly, the post-implantation injury occurs as the rigid Si microelectrode keeps cutting the surrounding soft tissues like a knife.

Current methods to overcome the technical barrier include fabricating small-size electrodes to reduce the tissue damage, selecting biocompatible and flexible polymeric materials to match the mechanical properties of brain, and integrating various drug delivery systems into the electrode to suppress the reactive tissue response.[6–8] However, small-size electrode definitely has higher impedance to degrade the signal quality, and it is difficult to insert the flexible polymer electrode into the

*Author to whom correspondence should be addressed.

cortical tissue without the help of special tools which usually generate additional tissue damage.[9] In addition, cumbersome pumping system is normally needed for drug delivery via microfludic channels. Therefore, issues associated with extra tissue damage and potential infection have to be considered in this case.

Our strategy to solve the technical challenge is to design and fabricate a novel porous Si (PSi)-polymer hybrid microelectrode consisting of a PSi backbone, polymer insulating layers and gold recording sites. The PSi backbone (~ 50 μm in thickness) cannot only provide enough stiffness to penetrate into the cortical tissue, but also serve as the reservoir to store the anti-inflammatory drugs (to minimize the reactive tissue response) and/or biomoleculars (to promote neuron growth). With the gradual degradation of the PSi backbone, the drugs and/or biomoleculars are delivered to surrounding tissues. More importantly, the remaining polymer insulating layers (~ 10 μm in thickness) and the in-between metallization (~ 500 nm in thickness) maintain flexibility and have mechanical properties similar to those of the cortical tissue, to reduce the post-implantation injury.

Nanostructured PSi has emerged over the past several years as a promising and multifunctional material for optical, electrical and biomedical applications.[10–13] Although nano features of PSi has been taken into account by a previous study to suppress astrocyte adhesion on a neural microelectrode,[14] research to date has not taken advantage of the biodegradability and drug delivery capability of PSi to establish the stable neural interface. As the first critical step to manufacture the PSi-polymer hybrid neural microelectrode, 70 μm-thick PSi layer were prepared on an 8-inch Si wafer via an anodization process. Subsequently, surface characteristics, biodegradability and *in vitro* biocompatibility of the PSi were investigated as fundamental research to prove the concept of the novel neural microelectrode. The knowledge obtained in this investigation is expected to be applicable to both the microfabrication and characterization of the novel neural microelectrode.

2. MATERIALS AND METHODS

2.1. Sample Preparation

P-type (boron doped) 8-inch (100) silicon wafers with resistivity of 0.002∼0.005 Ω cm (Sumco Corp., Japan) were cleaned using the standard piranha procedure. The blank Si wafer was then anodized in a mixed electrolyte solution of hydrofludic acid and ethanol (volume ratio, 1:1), at a current of 3.5 A for 120 min. As a consequence, a PSi layer (70 μm thick) was produced. Subsequently, the anodized Si wafer was cut into plates (7 mm × 7 mm). To compare the surface characteristics, biodegradability, *in vitro* biocompatibility of samples, Si plates (7 mm × 7 mm) with the same dimension as PSi samples were prepared as the control by dicing blank Si wafers.

2.2. Surface Characterization

A field emission scanning electron microscope (FE-SEM, JSM-6700F, JEOL, USA) was used to observe surface morphology of Si and PSi samples. Porous structure of the PSi layer was characterized using a field emission analytic transmission electron microscope (FEG-TEM, CM200, FEI/Philips Electron Optics, Netherlands). Surface wettability of Si and PSi samples was assessed by means of the sessile drop method, using a contact angle goniometer (DSA 100, KRÜSS, Germany).[15] 2 μl of distilled water was dropped on the surface of samples.

2.3. Biodegradability

Biodegradability of PSi samples was evaluated by an ammonium molybdate colorimetric assay. Briefly, 42 mM ammonium molybdate (Amoly) solution prepared by dissolving ammonium heptamolybdate tetrahydrate salt in distilled water was acidified by mixing with 0.3 M HCl in ratio of 1:2 by volume. 1.35 M sodium sulphite solution and 50 mM EDTA solution were prepared by dissolving anhydrous sodium sulphite salt and EDTA disodium salt into distilled water (DIW), respectively. Si or PSi samples were immersed in 1 ml of DIW at 37 °C. At predefined time intervals, 200 μl of DIW containing the degradation product of samples was then added into 50 μl Amoly/HCl solution, followed by vortex for 3 sec and incubation for 10 min. Subsequently, 25 μL of EDTA solution was added into the mixture. After vortex for 3 sec and incubation for 5 min, 25 μl of sodium sulphite was then blended with the mixed solution. Finally, the solution was aged at room temperature for 1 h and its absorbance was measured using a microplate reader (DTX 800 Series Multimode Detectors, Beckman Coulter, CA) at 600-nm wavelength. All assays were performed in triplicate.

2.4. *In Vitro* Biocompatibility Assessment

2.4.1. Cell Culture

A breast cancer cell line (MCF-7, ATCCHTB-22) was used to assess *in vitro* biocompatibility of the PSi due to its well-established model,[16–18] and was cultured in Dulbecco's Modified Eagle Medium (DMEM) (Invitrogen Co. USA) supplemented by 10% (v/v) fetal bovine serum (FBS) (Biowest, France). After being incubated at 37 °C in an atmosphere of 5% CO_2 and 95% humidity and reaching 75∼80% confluence, they were detached by 0.25 (w/v) trypsin-ethylenediaminetetraacetic acid (trypsin-EDTA) (Invitrogen) and counted by an automated cell counter (Luna™, Logos Biosystems, USA).

2.4.2. Live/Dead Assay

MCF-7 cells were seeded at 2.0×10^4 cells/well and cell viability of samples was determined by live/dead cytotoxicity assay.[19] Si samples and latex served as the negative and positive control in the assay, respectively. Living cells were stained in green via the

enzymatic conversion of the virtually nonfluorescent cell-permeant calcein-AM to the intensely fluorescent calcein (excitation/emission, ~495 nm/~515 nm), while EthD-1 entered cells with damaged membranes and produced a bright red fluorescence in dead cells (excitation/emission,~495 nm/~635 nm) after binding to nucleic acids. After 5 days of culture, MCF-7 cells stained in green and red were observed using a fluorescence microscope (Olympus BX61, Olympus Optical Co., Japan). Cell viability was calculated by normalizing the number of living cells with the total number of cells on the surface of samples. In order to calculate the cell viability, stained cells were counted under 200× magnification from at least seven randomly chosen areas on each sample.

2.4.3. MTT Assay

Proliferation of MCF-7 cells on Si and PSi samples was evaluated via 3-(4,5-dimethylthiazol-2-yl)-2,5-diphenyltetrazolium bromide (MTT) assay.[20, 21] MCF-7 cells were seeded onto tissue culture polystyrene (TCP, as the negative control), Si, PSi and latex (positive control), respectively. At each time point, 20 μL of MTT solution was added into each well and then the 48-well cell culture plate containing samples was stored in a cell culture incubator with 5% CO_2 at 37 °C for 4 hours. Subsequently, 100 μL dimethyl sulfoxide (DMSO) was added into each well to dissolve the formed formazan as a resolvent. Finally, absorbance was recorded using a microplate reader (DTX 800 Series Multimode Detectors, Beckman Coulter, USA) at 570 nm wavelength, with a reference wavelength of 640 nm to evaluate the proliferation of MCF-7 cells on samples in comparison to the control.

2.5. Statistical Analyses

All experiments were performed at least three times and all values are expressed as means ± standard errors. The data were compared using one-way analysis of variance (ANOVA) followed by the Tukey's test. $P < 0.05$ was considered to be statistical significance.

3. RESULTS AND DISCUSSION

3.1. Surface Characteristics

Figure 1 shows the surface morphology of Si and PSi samples. The surface of Si samples was uniform and smooth (Fig. 1(a)), while irregular pores with the dimension less than 20 nm were clearly visible under SEM due to the anodization of the Si wafer (Fig. 1(b)), and homogeneously distributed across the surface. Compared to those of Si, mechanical properties of PSi, depending on its porosity, are degraded due to the formation of the porous structure. It was reported that the pore size were controllable by tuning wafer doping level and type, anodization current density and electrolyte composition.[22–24] In this research, the pore size was controlled via anodization current density, and the criteria to optimize the pore size include enough mechanical strength to penetrate into cortical tissue, biodegradability and drug loading capability. Using the current parameters, the PSi backbone has been successfully fabricated, and its mechanical properties, drug loading capability and biodegradability have been being evaluated.

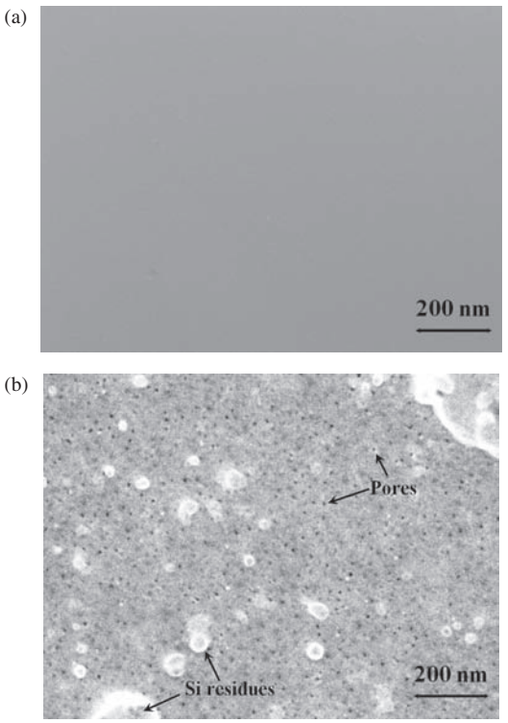

Figure 1. Surface morphology of (a) Si and (b) PSi samples.

The bright-field cross sectional TEM image of the PSi layer shows a mixture of bright and black speckles like a disordered network (Fig. 2). The bright regions, ranging from 2 to 20 nm in diameter, indicated the interconnected porous structure with irregular pore shapes, which was consistent with the results from SEM (Fig. 1(b)). On the

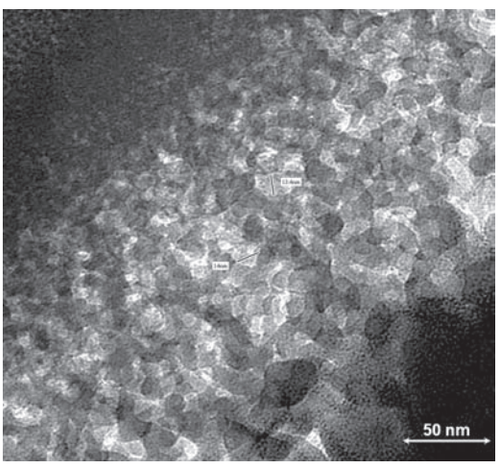

Figure 2. Bright-field TEM image of the PSi layer.

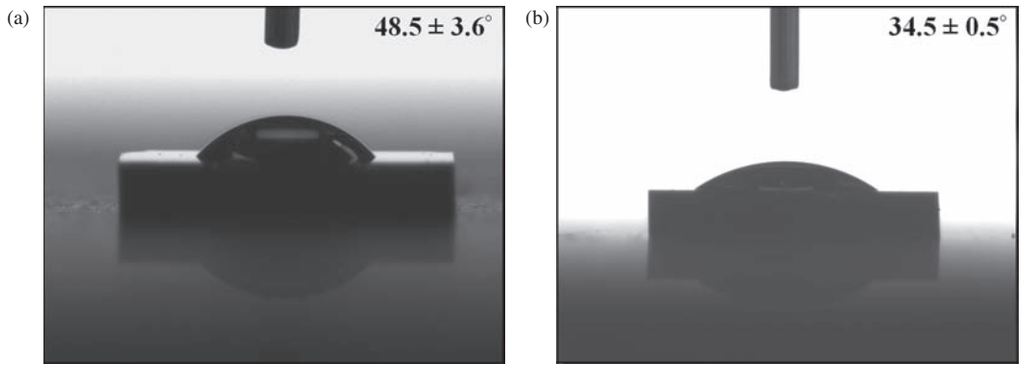

Figure 3. Water contact angles of (a) Si and (b) PSi samples.

contrary, the black speckles with nano-sized dimensions were Si nano crystallites. Jin et al. reported that the crystalline skeleton of the PSi had the same orientation as the Si substrate over the whole thickness of layers.[25]

Figure 3 illustrates the distilled water contact angles of Si and PSi samples. Si samples possessed moderately hydrophilic surface with a water contact angle of 48.5 ± 3.6° (Fig. 4(a)), which was in agreement with previous results. Kown et al. reported that water contact angle of *p*-type (100) Si substrate was 51°.[26] A study conducted by

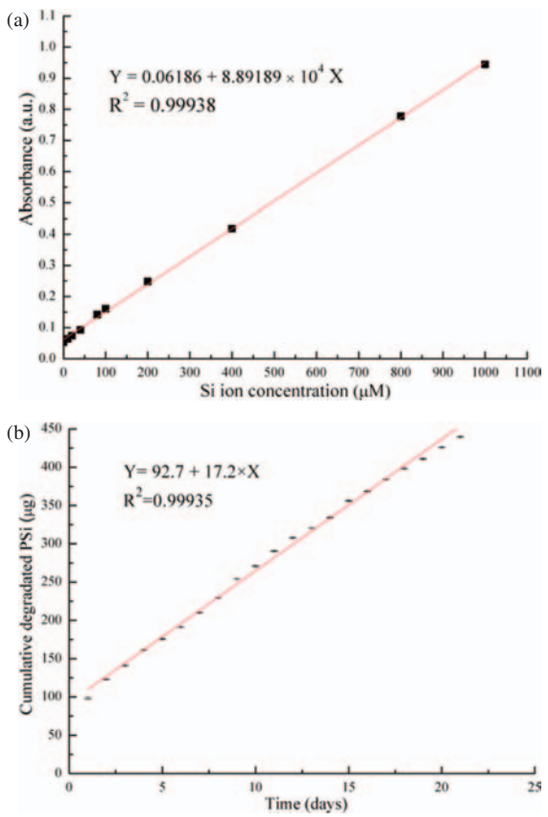

Figure 4. (a) Calibration curve of Si ion concentration in DIW; (b) degradation profiles of Si and PSi samples incubated in DIW for 21 days.

Roy et al. showed the similar results.[27] After the anodization process, wettability of PSi samples was improved since its water contact angle reduced to 34.5 ± 0.5° ($p < 0.05$). It was believed that wettability of PSi samples was mainly determined by its surface chemical composition, surface roughness and the capillary effect generated by nano sized pores. Therefore, a wide range of water contact angles on PSi was reported due to the factors above mentioned.

The mechanism of PSi formation can be described by Eq. (1), where h^+ represents holes in the Si valence band.[22] However, the surface of freshly prepared PSi is passivated and dominated by relatively stable Si–H_x functional groups ($x = 1$, 2 and 3), as Si–F on PSi surface is highly reactive and removed by HF electrolyte.[28] In contrast to Si–OH, Si–H terminated surface is hydrophobic in nature. High water contact angle (115°) was recorded for Si–H-terminated poly(dimethylsiloxane).[29] Similarly, Chen et al. reported that contact angle of the bare Si–H surface was around 90°.[30]

$$\mathrm{Si} + 6\mathrm{F}^- + 2\mathrm{H}^+ + 2h^+ \rightarrow \mathrm{SiF}_6^{2-} + \mathrm{H}_2 \qquad (1)$$

Besides surface chemical composition, water contact angle of PSi also depends on surface nano features. As shown in the following Eq. (1), Wenzel model establishes a relationship of the contact angles between a rough surface (θ_{rough}) and a smooth surface (θ_{smooth}) with identical surface chemistry via a roughness factor (γ, $\gamma > 1$).[31] Larger surface roughness attributes to a greater area fraction for the contact between the solid and liquid. Therefore, surface will become more hydrophilic with increasing surface roughness, according to Wenzel model. In this study surface of PSi samples was roughened after the anodization process (Fig. 1). Moreover, the effect of capillary force on water contact angle is also responsible for the enhanced wettability. Since the capillary force is inversely proportional to the pore size, the nano porous structure on the surface of PSi samples could generate significant capillary effect that reduced the water contact angle.[32] Therefore, water contact angle of PSi samples decreased due to the combination effect of Si–H_x

functional groups on the surface, rough surface, capillary force of nano sized pores.

$$\cos\theta_{\text{rough}} = \gamma \cos\theta_{\text{smooth}} \quad (2)$$

The improved wettability is thought to not only facilitate drug incorporation by means of soaking PSi samples into the aqueous solution of water-soluble drugs, but also promote cell attachment and proliferation for the reasons that most of cells exhibited a strong preference for hydrophilic substrates (but surface hydrophobicity is not the only determinant of cell attachment and proliferation).[33] Compared to bare hydrophobic poly(lactide-*co*-glycolide) acid (PLGA) surface, increased 3T3 fibroblast cell adhesion was clearly visible on glatin-chitosan immobilized PLGA surface with better wettability.[34] Additionally, more neuronal cells (PC12) adhered and generated neuritis on OH-terminated hydrophilic surface.[35]

3.2. Biodegradability

Calibration curve of Si ion concentration in DIW is shown in Figure 4(a). In aqueous solutions, the native SiH_x functional groups on PSi surface and bulk Si with porous nano-structure and high ratio of surface area to volume are spontaneously oxidized into soluble SiO_2 (Eqs. (3) and (4)), and final degradation products are composed of various silicic acid compounds with the orthosilicate (SiO_4^{4-}) ion as the basic building block (Eq. (5)).[36] Although $Si(OH)_4$ is toxic in high dose, it was the natural form of Si found in the body and could be excreted by kidneys. As shown in Figure 4(a), Si ion concentration in DIW is proportional to the intensity of the absorption at 600-nm wavelength, and the relationship was established by fitting a regression equation ($Y = 0.06186 + 8.89189 \times 10^4$ X, $R^2 = 0.99938$). Therefore, at each time point the linear behavior was used to extrapolate Si ion concentration in DIW from the measured absorbance by the simplifying assumption that variation of the absorbance is mainly induced by Si ion concentration.

$$SiH_x + H_2O \rightarrow SiO_2 + 4H_2 \quad (3)$$

$$Si + O_2 \rightarrow SiO_2 \quad (4)$$

$$SiO_2 + 2H_2O \rightarrow Si(OH)_4 \quad (5)$$

Figure 4(b) shows biodegradation profiles of PSi samples as the function of incubation time. The content of Si ion in DIW had liner relationship with the incubation time. As the biodegradation curve of PSi samples was fit by a liner equation ($Y = 92.7 + 17.2\times$ X, $R^2 = 0.99935$), the biodegradation rate was higher at day 1 (98.1 ± 1.2 μg), and then became relatively steady until 21 days (17.1 ± 3.8 μg/day). In addition, the accumulative Si content did not reach a constant value within 3-week incubation, but increased at the uniform biodegradation rate, indicating that PSi samples did not fully degrade in DIW. In our microelectrode design, PSi backbone should fully degrade after insertion into the cortical tissue, and its degradation period could be tuned by designing different sizes. In this study, the biodegradability of the raw materials was demonstrated and degradation rate was investigated via the ammonium molybdate colorimetric assay.

3.3. Live/Dead Assay

In order to minimize the number of animals in *in vivo* studies, *in vitro* investigation as the first step to evaluate biocompatibility of the PSi is essential to carry out, based on ISO 10993-5: 2009. In this study, *in vitro* biocompatibility of PSi samples was assessed in terms of cell morphology, cell viability and cell proliferation (MTT assay). Figures 5(a)–(c) show the morphology of MCF-7 cells seeded on latex, Si and PSi samples under the fluorescence microscope after 5 days of culture, respectively. Due to the

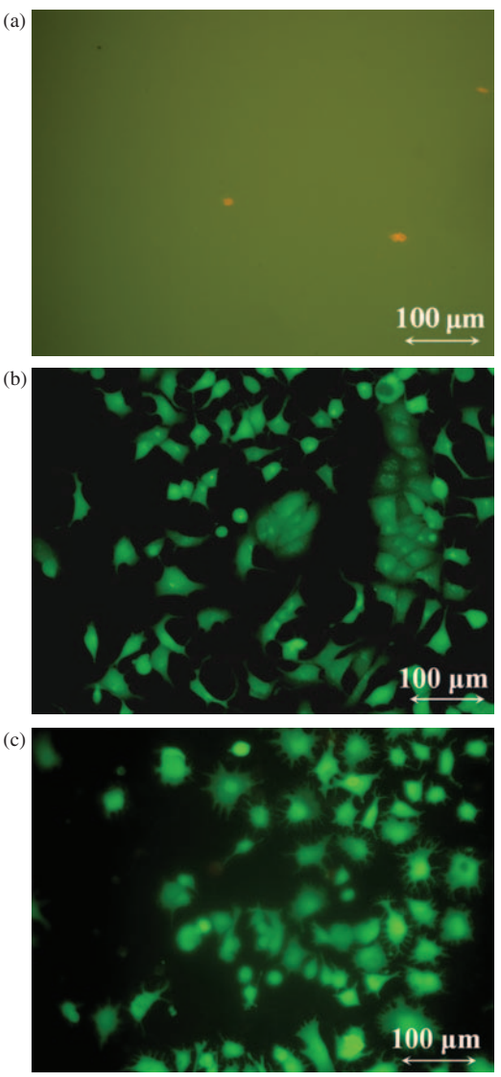

Figure 5. After 5 days of culture, morphology of MCF-7 cells seeded on (a) latex, (b) Si and (c) PSi samples.

preferred absorption of calcein-AM, the latex sample was stained in yellowish green under the fluorescence microscope (Fig. 5(a)). Few cells attached on its surface and were stained in red by EthD-1, indicating the cell death. On the contrary, at day 5 cells adhered to Si surface were flattened and spread extensively in all directions to form a polygonal configuration or spindle-like morphology (Fig. 5(b)). In addition, at some small and individual areas the cells appeared to grow into a subconfluent state. Compared to the cells seeded on Si, more cytoplasmic expansions or microfilaments protruded from the cellular body, anchoring cells to the PSi substrate (Fig. 5(c)). This phenomenon was ascribed to the rough PSi surface which provided more sites for cell adhesion. In addition, most of cells on PSi surface exhibited more round morphology or star-like morphology with the aspect ratio closer to 1, i.e., a prominent cell body surround by a flat and round cytoplasm. The cell viability was over 99% for Si and PSi samples at day 5, while no living cells were found on latex plates.

3.4. MTT Assay

To quantitatively evaluate *in vitro* biocompatibility of PSi samples in comparison with the control, MTT assay was performed since it is widely used to evaluate cytotoxcity and recommended by ISO 10993-5:2009.[37] The principle of MTT assay is the conversion of yellow tetrazolium salt by metabolically active cells into a purple formazan dye. Therefore, MTT assay is a highly sensitive, reproducible, fast, cost-saving, quantitative approach to evaluate the cytotoxicity by the reactions with living and metabolically active cells, instead of dead cells. Since the MTT value is directly proportional to the number of living cells, a higher MTT absorbance indicates higher cell proliferation. Hence, the steady increase in MTT absorbance for TCP, Si and PSi samples over the cell culture period (2∼5 days) revealed a gradual increase of cell number on sample surface (Fig. 6). As shown in Figure 6, the difference of MTT absorbance between TCP and Si was not statistically significant during the whole cell culture period ($P > 0.05$), revealing that Si samples were as cytocompatible as TCP and could serve as the negative control in *in vitro* studies. In contrast, the MTT value of latex samples, most likely resulting from living cells far away from the samples at the brim of the cell culture well, maintained the lowest level among all types of samples over the whole cell culture period due to the cytotoxicity ($P < 0.05$). Additionally, the MTT absorbance of PSi samples was always significantly higher than that of Si samples from day 2 to day 5, suggesting that the cytocompatibility of PSi was even better than that of Si. During MTT assay, needle-shaped formazan forms on the bottom of cell culture well and is visible under the optical microscope, when the tetrazolium salt (MTT) is reduced into formazan. In order to confirm the MTT results regarding the comparison between Si and PSi samples, at day 2 optical images for TCP, Latex, Si and PSi samples without and with cells were recorded after adding MTT solution for 4 hours. As shown in Figure 7(a), no needle-like formazan was formed for TCP without cells, whereas purple formazan was present in Figure 7(b) due to the conversion of tetrazolium salt by living cells. Interestingly, the needles were observed for PSi samples both without and with cells (Fig. 8), indicating that PSi had the same function as the living cells to spontaneously reduce tetrazolium salt into formazan. It was reported that MTT was

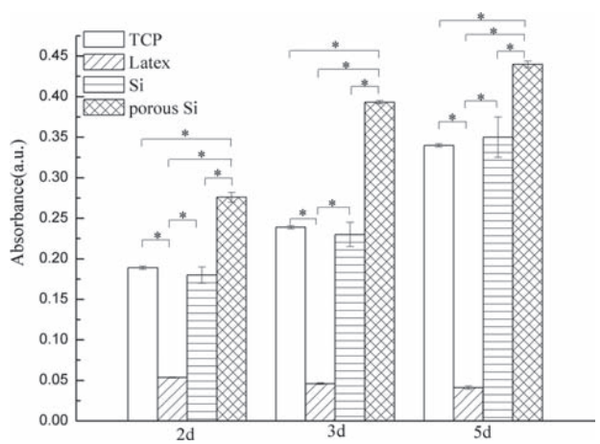

Figure 6. MTT assay of MCF-7 cells seeded on TCP, latex, Si and PSi samples after 2, 3 and 5 days of cell culture. The statistical significance is indicated by $^{*}(P < 0.05)$.

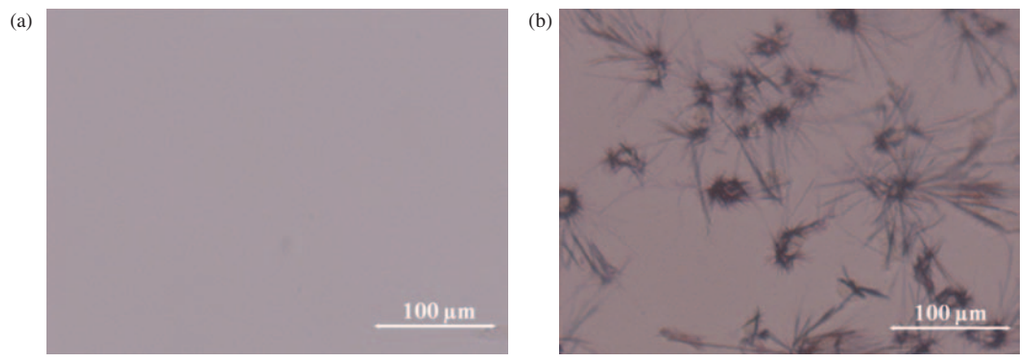

Figure 7. After adding MTT solution and incubation for 4 hours, optical images of TCP (a) without MCF-7 cells, (b) with MCF-7 cells.

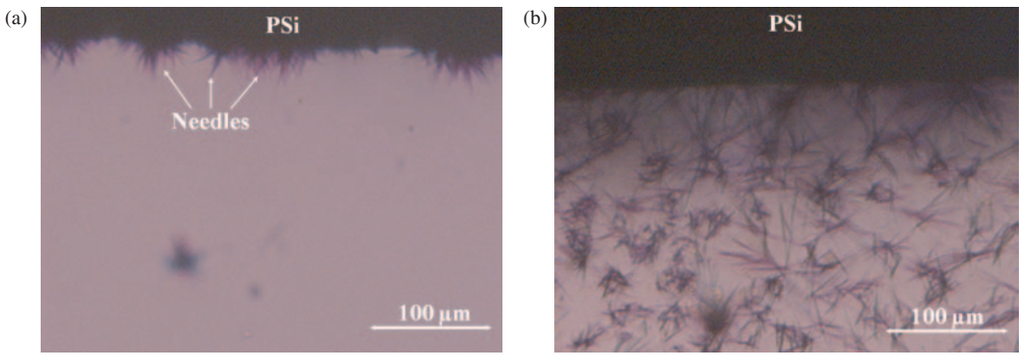

Figure 8. After adding MTT solution and incubation for 4 hours, optical images of PSi samples (a) without MCF-7 cells, (b) with MCF-7 cells.

reduced by corrosion products of Mg alloys in the absence of cells.[38] The midpoint potential of MTT is −110 mV, while that of SiH_4 is less than −2 V.[39] As a indicator of the strength of an electron donor, the midpoint potential can be defined as the voltage where equilibrium is obtained between the concentration of oxidized and reduced products, i.e., a more negative midpoint potential, a stronger electron donor. According to the midpoint potentials, the SiH_x functional groups and SiH_4 are capable of spontaneously reducing the yellow tetrazolium salt into the purple formazan end product to disrupt results from the MTT assay. Therefore, PSi interfered with MTT assay due to the spontaneous reduction of MTT. More appropriate quantitative *in vitro* assessments without false positive results should be investigated for the cytotoxicity of PSi samples. A DNA assay might be an alternative method to replace MTT assay.[40] The principle of the DNA assay is to use the fluorochrome bisbenzimid which changes the emission wavelength after intercalating with DNA. Then the intensity of the emitted fluorescence can be detected by a fluorometer, and is proportional to the amount of DNA and the number of living cells. Moreover, a commercial kit named "cell proliferation ELISA, BrdU Kit" will be evaluated in future studies as well. The mechanism of the measurement is based on luminescence rather than absorption, and takes advantage of a luminescent molecule binding into DNA. But the large surface to volume ratio (500 m^2/cm^3) of PSi might result in the adsorption of luminescent molecule onto the inner surface of PSi, and therefore influence the precision.

4. CONCLUSIONS

PSi layer with 3D interconnected and nano sized pores was prepared by the anodization process, and its water contact angle decreased to $34.5 \pm 0.5°$ in comparison with Si ($48.5 \pm 3.6°$). The factors to influence water contact angle of the PSi were proposed and discussed. To demonstrate the concept of the neural microelectrode design, biodegradability and biocompatibility of the PSi were investigated in DIW for 21 days and by seeding MCF-7cells, respectively. The biodegradation curve of the PSi in 1 ml of DIW was fit by the regression equation ($Y = 92.7 + 17.2 \times X$, $R^2 = 0.99935$), indicating that within 21 days the degradation rate was uniform except the first day and PSi samples were not fully degraded. The cell viability determined by live/dead assay was over 99% for both Si and PSi, but cell morphology on PSi samples was obviously distinct from that on Si likely due to surface nano features. MTT assay was carried out to quantitatively evaluate cell proliferation on samples. However, results from optical images confirmed that MTT could be spontaneously reduced by both PSi and living cells. Therefore, PSi interfered with the MTT assay, resulting in false positive results. *In vitro* biocompatibility of PSi should be quantitatively studied by other more appropriate methods.

Acknowledgments: The authors gratefully acknowledge staffs in the Bioelectronics Lab, Institute of Microelectronics for their generous help and valuable suggestions. This work was supported by the Science and Engineering Research Council of Agency for Science, Technology and Research (A*STAR) under Grant 1021710159, and also by Basic Science Research Program through the National Research Foundation of Korea (NRF) funded by the Ministry of Science, ICT and Future Planning (NRF-2013R1A1A1012616).

References and Notes

1. J. Wessberg, C. R. Stambaugh, J. D. Kralik, P. D. Beck, M. Laubach, J. K. Chapin, J. Kim, S. J. Biggs, M. A. Srinivasan, and M. A. L. Nicolelis, *Nature* 408, 361 **(2000)**.
2. J. K. Chapin, *Nat. Neurosci.* 7, 452 **(2004)**.
3. L. R. Hochberg, M. D. Serruya, G. M. Friehs, J. A. Mukand, M. Saleh, A. H. Caplan, A. Branner, D. Chen, R. D. Penn, and J. P. Donoghue, *Nature* 442, 164 **(2006)**.
4. J. L. Collinger, B. Wodlinger, J. E. Downey, W. Wang, E. C. Tyler-Kabara, D. J. Weber, A. J. C. McMorland, M. Velliste, M. L. Boninger, and A. B. Schwartz, *Lancet* 381, 557
5. J. D. Simeral, S. P. Kim, M. J. Black, J. P. Donoghue, and L. R. Hochberg, *Journal of Neural Engineering* 8 **(2011)**.
6. J. P. Seymour and D. R. Kipke, *Biomaterials* 28, 3594 **(2007)**.
7. A. Mercanzini, K. Cheung, D. L. Buhl, M. Boers, A. Maillard, P. Colin, J.-C. Bensadoun, A. Bertsch, and P. Renaud, *Sensors and Actuators A: Physical* 143, 90 **(2008)**.

8. C. T. Lo, P. R. Van Tassel, and W. M. Saltzman, *Biomaterials* 30, 4889 **(2009)**.
9. L. Spataro, J. Dilgen, S. Retterer, A. J. Spence, M. Isaacson, J. N. Turner, and W. Shain, *Experimental Neurology* 194, 289 **(2005)**.
10. P. J. Ko, R. Ishikawa, H. Sohn, and A. Sandhu, J. *Nanosci. Nanotech.* 13, 2451 **(2013)**.
11. S. Um, S. G. Lee, H.-G. Woo, S. Cho, and H. Sohn, *J. Nanosci. Nanotech.* 13, 288 **(2013)**.
12. P. J. Ko, R. Ishikawa, T. Takamura, Y. Morimoto, B. Cho, H. Sohn, and A. Sandhu, *Nanosci. Nanotech. Lett.* 3, 612 **(2011)**.
13. D. Prabhakar, V. Kumari, and S. S. Islam, *Sci. Adv. Mater.* 4, 121 **(2012)**.
14. K. A. Moxon, N. M. Kalkhoran, M. Markert, M. A. Sambito, J. L. McKenzie, and J. T. Webster, *IEEE Transactions on Biomedical Engineering* 51, 881 **(2004)**.
15. T. Sun, W.-C. Lee, and M. Wang, *Mater. Lett.* 65, 2575 **(2011)**.
16. T. Sun, L.-P. Wang, M. Wang, H.-W. Tong, and W. W. Lu, *Mater. Sci. Eng., C* 32, 1469 **(2012)**.
17. H. K. Dhiman, A. R. Ray, and A. K. Panda, *Biomaterials* 26, 979 **(2005)**.
18. T. Sun, M. Wang, and W.-C. Lee, *Mater. Chem. Phys.* 130, 45 **(2011)**.
19. K. Buyukhatipoglu, T. A. Miller, and A. M. Clyne, *J. Nanosci. Nanotech.* 9, 6834 **(2009)**.
20. N. Sultana and M. Wang, *Biofabrication* 4 **(2012)**.
21. D. Guo, C. Wu, X. Li, H. Jiang, X. Wang, and B. Chen, *J. Nanosci. Nanotech.* 8, 2301 **(2008)**.
22. R. L. Smith and S. D. Collins, *J. Appl. Phys.* 71, R1 **(1992)**.
23. M. Miu, M. Danila, I. Kleps, A. Bragaru, and M. Simion, *J. Nanosci. Nanotech.* 11, 9136 **(2011)**.
24. E. Haimi, V. K. Lindroos, and R. Nowak, *J. Nanosci. Nanotech.* 1, 201 **(2001)**.
25. S. Jin, H. Bender, L. Stalmans, R. Bilyalov, J. Poortmans, R. Loo and M. Caymax, *J. Cryst. Growth* 212, 119 **(2000)**.
26. Y. B. Kwon, B. M. Weon, K. H. Won, J. H. Je, Y. Hwu, and G. Margaritondo, *Langmuir* 25, 1927 **(2009)**.
27. R. K. Roy, H.-W. Choi, S.-J. Park, and K.-R. Lee, *Diamond and Related Materials* 16, 1732 **(2007)**.
28. A. Tzur-Balter, A. Gilert, N. Massad-Ivanir, and E. Segal, *Acta Biomaterialia* 9, 6208 **(2013)**.
29. M. K. N. Hirayama, W. R. Caseri, and U. W. Suter, *J. Colloid Interface Sci.* 216, 250 **(1999)**.
30. R. Chen, H. Kim, P. C. McIntyre, D. W. Porter, and S. F. Bent, *Appl. Phys. Lett.* 86 **(2005)**.
31. R. N. Wenzel, *Ind. Eng. Chem.* 28, 988 **(1936)**.
32. R. A. Fleming and M. Zou, *Appl. Surf. Sci.* 280, 820 **(2013)**.
33. Y. Arima and H. Iwata, *Biomaterials* 28, 3074 **(2007)**.
34. A. P. Zhu, N. Fang, M. B. Chan-Park, and V. Chan, *Biomaterials* 27, 2566 **(2006)**.
35. G. Lamour, A. Eftekhari-Bafrooei, E. Borguet, S. Souès, and A. Hamraoui, *Biomaterials* 31, 3762 **(2010)**.
36. E. J. Anglin, L. Cheng, W. R. Freeman, and M. J. Sailor, *Advanced Drug Delivery Reviews* 60, 1266 **(2008)**.
37. T. Sun, W.-T. Park, M.-Y. Cheng, J.-Z. An, R.-F. Xue, K.-L. Tan, and M. Je, *IEEE Transactions on Biomedical Engineering* 59, 390 **(2012)**.
38. J. Fischer, M. H. Prosenc, M. Wolff, N. Hort, R. Willumeit, and F. Feyerabend, *Acta Biomaterialia* 6, 1813 **(2010)**.
39. J. Lalevee, N. Blanchard, M.-A. Tehfe, and J. P. Fouassier, *Macromol. Rapid Commun.* 32, 838 **(2011)**.
40. C. Labarca and K. Paigen, *Anal. Biochem.* 102, 344 **(1980)**.

Received: 17 September 2013. Accepted: 21 November 2013.